

Modeling of vortex ripple morphodynamics

V. Marieu,^{1,2} P. Bonneton,^{1,2} D. L. Foster,³ and F. Arduin⁴

Received 23 November 2007; revised 7 May 2008; accepted 12 June 2008; published 4 September 2008.

[1] A new morphology module has been developed in order to perform simulations of the bed form evolution under hydrodynamic forcing. This module has been implemented into the numerical model Dune2D, which solves the Reynolds Averaged Navier-Stokes (RANS) equations in the boundary layer and resolves sediment transport over moving sand beds. The morphology module is composed of a modified central scheme and a routine that simulates avalanches and has been successfully applied to the study of orbital ripples evolution. Ripple growth from a quasiflat bed have been simulated, and the growth behavior has been compared to previous experimental measurements. The simulated ripples reach an equilibrium state where energy damping processes (avalanches) compensate energy production processes (flux of sediment). These processes have been analyzed during ripple creation, growth, merging, and annihilation. Furthermore, sandy bed evolutions have been simulated with random initial bed forms in order to examine the influence of the bed “history” on the final solution and the wave energy dissipated during these evolutions.

Citation: Marieu, V., P. Bonneton, D. L. Foster, and F. Arduin (2008), Modeling of vortex ripple morphodynamics, *J. Geophys. Res.*, 113, C09007, doi:10.1029/2007JC004659.

1. Introduction

[2] The interaction between wave-induced coastal flows and sandy seafloors results in the formation and evolution of an array of bed forms. Ripples are among the smallest scale of these bed forms. Ripples impact the distribution of mean flows, the propagation of waves, and the transport of sediment, either by their migration or by the vortex shedding induced suspension. The nearbed turbulence induced by the vortex generation can also enhance water and nutrient fluxes in the sediment layer, with an impact on the carbon cycle [Precht *et al.*, 2004]. Waveformed ripples have been studied for centuries. Both Darwin [1883] and Bagnold [1946] characterized “vortex ripples” as bed forms with vortices formed at the lee of the ripple crest and ejected upward during each flow reversal. Since then, vortex ripple formation and evolution have been studied in the course of laboratory experiments and field observations. With a range of field observation and experimental data, Clifton and Dingle [1984] separated vortex ripples in three classes. Orbital ripples have wavelengths, λ_r , linearly dependent on the wave orbital excursion near the bed, A_0 . Anorbital ripples have wavelengths that only depend on the grain diameter, d . Suborbital ripples are an intermediate stage where ripples wavelength depends both on the wave orbital

excursion and on the grain diameter. Wiberg and Harris [1994] proposed a ripple geometry predictor based on this classification. Alternative ripple predictors also consider the wave period, the fluid and sediment [Nielsen, 1981; Grant and Madsen, 1982; van Rijn, 1993].

[3] Despite support through several laboratory studies, these predictors have limitations. Some observations show wavelengths with up to one order of magnitude difference from the predicted wavelength [Nielsen, 1981; Wiberg and Harris, 1994; Soulsby and Whitehouse, 2005]. Moreover, some large orbital ripples have been observed in the supposedly anorbital ripple range [Traykovski *et al.*, 1999; Arduin *et al.*, 2002]. Finally, these predictor models are limited to reasonably simple forcing conditions and do not resolve formations such as squash ripples, long wavelength ripples, megaripples, etc. [Soulsby and Whitehouse, 2005].

[4] Ripple formation and evolution have also been studied with theoretical models [Blondeaux, 1990; Vittori and Blondeaux, 1990] or one-dimensional models [Andersen *et al.*, 2001]. These models predict ripple behavior and are simple to implement, but full two-dimensional models are necessary to resolve the vortex generation and evolution above a rippled bed. Two-dimensional numerical simulation have primarily been used for hydrodynamics, sediment concentrations and fluxes calculations [Andersen, 1999; Foster *et al.*, 2001; Zedler and Street, 2001; Chang and Hanes, 2004; Li and O'Connor, 2007]. True flow and morphologic coupling has been limited because of numerical limitations in the sediment conservation equation, which links the sediment fluxes to the bed height (assuming nonlinear formulations are used for the sediment fluxes calculation). This is particularly relevant in the case of vortex ripples where the slope variation at the crest of the ripples represents a discontinuity which is difficult to solve

¹Université Bordeaux 1, UMR 5805-EPOC, Talence, France.

²CNRS, UMR 5805-EPOC, Talence, France.

³Department of Civil and Environmental Engineering and Geodetic Science, Ohio State University, Columbus, Ohio, USA.

⁴Service Hydrographique et Océanographique de la Marine, Brest, France.

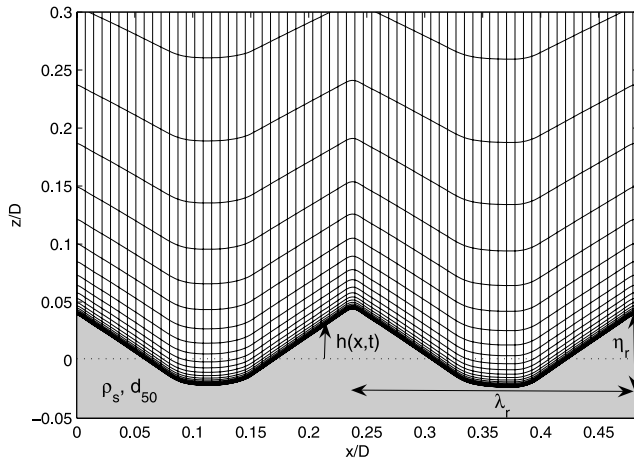


Figure 1. Dune2D 200×30 computational grid used for the simulations over two orbital ripples, one of three grid cells plotted in x direction.

numerically because it can induce instabilities [Johnson and Zyserman, 2002]. These instabilities can be artificially smoothed, however, the smoothing may prevent the evolution of small perturbations and bed evolution from a quasiflat bed.

[5] This paper presents a new morphologic approach to resolve bed form evolution that is based on a modified nonoscillatory central scheme for ripple growth and slope avalanching. This approach leads to an equilibrium between building processes and damping processes, allowing the bed to reach a saturation state when submitted to a regular forcing. This morphology module has been integrated into an existing flow and sediment transport model, Dune2D [Tjerry, 1995; Andersen, 1999; Fredsøe and Tjerry, 2001] to perform simulations of vortex ripple growth and evolution.

2. Governing Equations and Dune2D Model

[6] Dune2D is a two-dimensional bottom boundary layer model which was first developed by Tjerry [1995] to simulate flow over noncohesive sediment beds in alluvial rivers and to examine the bed response to this flow. Andersen [1999] added the oscillatory forcing component in order to simulate the flow induced by waves.

[7] For these simulations, the model is forced over the entire domain by the horizontal pressure gradient parameterized with linear wave theory with

$$\frac{\partial P}{\partial x} = -\rho\omega_0 U_0 \cos(\omega_0 t). \quad (1)$$

where P is the pressure, ρ the fluid density, U_0 the free stream orbital velocity near the top of the boundary layer, and $\omega_0 (=2\pi/T)$ is the wave angular frequency, where T is the wave period. Figure 1 shows an example of the boundary-fitted transfinite grid. The flow is computed above the bed form height h . The domain depth, D , is selected large enough to ensure that it does not have an influence on the computed flow, therefore it does not represent the real boundary layer thickness or water depth [Andersen, 1999]. Following Nattoo [2003], we specify $D = U_0 T$. The grid is

generated by a boundary fitted transfinite interpolation method [Eriksson, 1982] after each morphological calculation. In order to deal with the boundary condition at bed, the grid cell thickness immediately next to the bed is set to $2\nu/u^*$ [Andersen, 1999], where ν is the kinematic viscosity of water and u^* is the friction velocity on a flat bed. The upper boundary is closed by a rigid-lid boundary condition and a cyclic boundary condition is set on the lateral sides of the domain. In the present study, the relative density is $s = \rho_s/\rho = 2.65$, corresponding to quartz sand, where ρ_s and ρ are respectively the sediment and fluid densities. d_{50} is the median grain size, and λ_r and η_r are respectively ripples wavelength and height (cf. Figure 1).

[8] More information about the model and numerical methods used in Dune2D is available in Tjerry [1995], Andersen [1999], and Tjerry and Fredsøe [2005].

2.1. Hydrodynamics

[9] The flow field is resolved with the two-dimensional Reynolds averaged Navier-Stokes equations (RANS). The averaged fluid velocity components, U_i , are the unknown, where $i = 1, 2$ represent the two space coordinates of the system $x_1 = x$ and $x_2 = z$. The governing equations are

$$\frac{\partial U_i}{\partial t} + U_j \frac{\partial U_i}{\partial x_j} = -\frac{1}{\rho} \frac{\partial P}{\partial x_i} + \frac{\partial}{\partial x_j} (2\nu S_{ij} + \tau_{ij}) \quad (2)$$

$$\frac{\partial U_i}{\partial x_i} = 0, \quad (3)$$

where P is the pressure, S_{ij} is the strain rate tensor, $S_{ij} = \frac{1}{2} (\frac{\partial U_i}{\partial x_j} + \frac{\partial U_j}{\partial x_i})$, and τ_{ij} is the Reynolds stress tensor given by

$$\tau_{ij} = -\overline{u'_j u'_i} = 2\nu_T S_{ij} - \frac{2}{3} k \delta_{ij} \quad (4)$$

where ν_T is the eddy viscosity, k is the kinetic energy, and u'_i is the fluctuating component of the velocity. Turbulence closure is achieved using the $k-\omega$ model developed by Wilcox [1988] which has been successfully applied to problems with strong adverse pressure gradients and rough wall boundary conditions [Bradshaw et al., 1996]. The quantities k and ω and the eddy viscosity $\nu_T = \gamma^* k/\omega$ are obtained by resolving the closure equations,

$$\frac{\partial k}{\partial t} + U_j \frac{\partial k}{\partial x_j} = \frac{\partial}{\partial x_j} \left[(\nu + \sigma^* \nu_T) \frac{\partial k}{\partial x_j} \right] - \overline{u'_i u'_j} \frac{\partial U_i}{\partial x_j} - \beta^* k \omega \quad (5)$$

$$\frac{\partial \omega}{\partial t} + U_j \frac{\partial \omega}{\partial x_j} = \frac{\partial}{\partial x_j} \left[(\nu + \sigma \nu_T) \frac{\partial \omega}{\partial x_j} \right] + \gamma \frac{\omega}{k} \left(-\overline{u'_i u'_j} \frac{\partial U_i}{\partial x_j} \right) - \beta \omega^2 \quad (6)$$

where $\beta = 3/40$, $\beta^* = 9/100$, $\sigma = 1/2$, $\sigma^* = 1/2$, $\gamma = 5/9$, and $\gamma^* = 1$ are the closure coefficients. The governing equations are discretized using a finite volume method with an ISNAS scheme [Zijlema, 1996]. A PISO (Pressure Implicit Splitting of Operators) algorithm is used to calculate the pressure [Patankar, 1980] and a process of iteration is applied to find the force necessary to drive the mean current (null if only

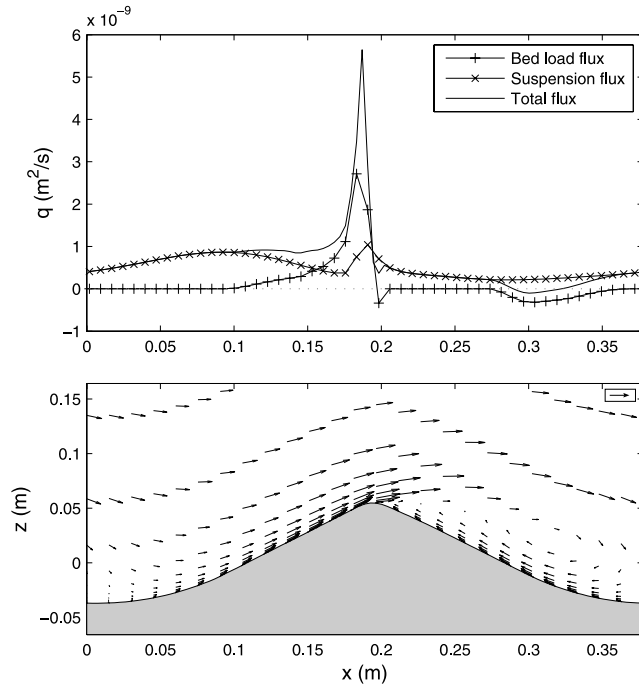


Figure 2. Instantaneous bed load, suspended load, total flux (upper), and velocity field (lower) over one vortex ripple at $t = T/4$. The free stream velocity is $U = U_0 \sin(\omega_0 t)$. A 0.25 m/s scale vector is shown in the upper right corner at the bottom.

waves are simulated), using a Proportional-Integral-Derivative control algorithm set by *Andersen* [1999].

2.2. Sediment Transport

[10] The total sediment transport includes contributions from the near bed load and the water column integrated suspended load. The bed load horizontal flux is calculated by the formulation of *Meyer-Peter and Müller* [1948] as follows

$$q_b(x, t) = 8(\theta(x, t) - \theta_{ca}(x))^{\frac{3}{2}}, \quad \theta(x, t) > \theta_{ca}(x) \quad (7)$$

$$q_b(x, t) = 0, \quad \theta(x, t) \leq \theta_{ca}(x)$$

or the formulation of *Engelund and Fredsøe* [1976],

$$q_b(x, t) = 5n(x, t) \left(\sqrt{\theta(x, t)} - 0.7\sqrt{\theta_{ca}(x)} \right), \quad \theta(x, t) > \theta_{ca}(x)$$

$$q_b(x, t) = 0, \quad \theta(x, t) \leq \theta_{ca}(x) \quad (8)$$

where θ is the Shields parameter, θ_{ca} is the slope corrected critical Shields parameter, as defined by *Fredsøe and Deigaard* [1992], and n is the fraction of the particles that may be in the upper layer of the bed. The Shields parameter represents the non dimensional shear stress at the bed, τ_b , and is given by

$$\theta(x, t) = \frac{\tau_b(x, t)}{\rho g (s - 1) d_{50}}. \quad (9)$$

The fraction of the particles that may be in the upper layer of the bed is calculated as follows

$$n(x, t) = \left[1 + \left(\frac{\frac{\pi}{6} \mu_d}{\theta(x, t) - \theta_{ca}(x)} \right)^4 \right]^{-\frac{1}{4}} \quad (10)$$

with μ_d , the dynamic friction on the bed.

[11] The formulation of Meyer-Peter and Müller (equation (7)) is generally employed for low stress values ($\theta < 1$) whereas the formulation of Engelund and Fredsøe (equation (8)) is more appropriated for higher shear stress values [*Nielsen*, 1992].

[12] The sediment concentration, c , is calculated with the advection-diffusion equation given by

$$\frac{\partial c}{\partial t} + u_j \frac{\partial c}{\partial x_j} = \frac{\partial w_s c}{\partial z} + \frac{\partial}{\partial x_j} \left(\nu_T \frac{\partial c}{\partial x_j} \right), \quad (11)$$

where w_s is the settling velocity defined with

$$w_s = \sqrt{\frac{4(s - 1)gd_{50}}{3C_D}}, \quad (12)$$

where C_D is the drag coefficient for natural sand. The bottom boundary condition for equation (11) is defined with a reference concentration model by *Engelund and Fredsøe* [1976] at $z = h + 2d_{50}$, where $z = 0$ is the mean bed height. The suspended load horizontal flux results from an integration over the water column of

$$q_s(x, t) = \int_{h(x, t)}^D c(x, z, t) u(x, z, t) dz. \quad (13)$$

2.3. Flow Morphologic Coupling

[13] The sediment transport and morphologic evolution are coupled through the sediment conservation equation

$$\frac{\partial h}{\partial t} + \frac{\partial q}{\partial x} = 0 \quad (14)$$

where h is the bed height and q is the total sediment flux given by

$$q = \frac{1}{1 - p} (q_b + q_s) \quad (15)$$

where p ($=0.4$) is the porosity of the bed.

[14] Figure 2 shows the velocity field and the sediment flux over one vortex ripple at the instant $t = T/4$ (maximum right-directed free stream velocity). The flow separation induced by the crest of the ripple generates a discontinuity of the term $\partial q / \partial x$. Consequently, the sediment conservation equation (14) is resolved with a shock-capturing scheme in order to preserve the mass flux on each side of the shock.

[15] Many morphological models assume a total flux function which directly depends on the bed form variations [*Callaghan et al.*, 2006]. In these models, the conservation equation (14) can be transformed into its nonconservative

form that describes an advection of the bed at a celerity $a = dq/dh$. A large number of hyperbolic schemes are available to solve this equation [Leveque, 2002]. In Dune2D, the sediment flux is not an explicit function of h . Instead, it is the result of the full hydrodynamic calculation, combined with a bed load formulation and a transport equation for the sediment in suspension, therefore the scheme has to solve the conservative form equation (14) of the sediment conservation equation.

[16] Initially, the scheme implemented in the morphology module of Dune2D was the Quadratic Upstream Interpolation for Convective Kinematics (QUICK) by Leonard [1979]. This scheme does not solve the conservative form of the sediment conservation equation and therefore requires a calculation of the bed celerity in order to perform an upwinding shift on the grid. Consequently, the QUICK scheme is not able to resolve the flux discontinuity at ripple crest and spurious oscillations can appear. By smoothing the flux, it is possible to avoid these oscillations, however, the resulting bed form shape is dependent on the filter characteristics. Furthermore, the filtering can prevent the small perturbations from developing and growing, hence ripple creation from a flat bed locally perturbed is impossible.

[17] A high order hyperbolic scheme, the weighted essentially nonoscillating (WENO) scheme by Liu et al. [1994] that has been successfully implemented in morphological calculations by Caleffi et al. [2006] and Long et al. [2008] was initially evaluated [Marieu, 2007]. The scheme only requires the sign of the local bed celerity, estimated with $sign(a) = sign(\Delta q/\Delta h)$. The WENO scheme performed very well on a simple advection test but, it is unable to resolve the flux discontinuity at ripple crest and it leads to spurious oscillations in the resulting bed form. In this effort, the family of nonoscillatory centered schemes (NOCS) developed by Nessyahu and Tadmor [1990] has been chosen. These schemes solve the conservative form of equation (14) and do not require the calculation of dq/dh .

2.4. Modified Nonoscillatory-Centered Scheme

[18] NOCS are second order natural extensions of the first-order Lax–Friedrich scheme. In the present study, we used a modified version of the staggered NOCS presented by Nessyahu and Tadmor [1990] which is more accurate than the nonstaggered NOCS. The bed elevation on a staggered grid is obtained at step $n + 1$ using a predictor–corrector method. The predictor step is used to calculate the total flux q at step $n + \frac{1}{2}$ for a grid node i using the first-order scheme

$$\begin{cases} h_i^{n+\frac{1}{2}} = h_i^n - \frac{1}{2} \frac{\Delta t}{\Delta x} q_i^n \\ q_i^{n+\frac{1}{2}} = q\left(h_i^{n+\frac{1}{2}}\right) \end{cases} \quad (16)$$

where q' is the approximate numerical derivative of the flux q , Δt and Δx are respectively the time and space steps. The corrector step is used to calculate the bed height at step $n + 1$, using the flux $q_i^{n+\frac{1}{2}}$ calculated during the predictor step

$$h_{i+\frac{1}{2}}^{n+1} = \frac{1}{2} (h_i^n + h_{i+1}^n) + \frac{1}{8} (h_i' - h_{i+1}') - \frac{\Delta t}{\Delta x} (q_{i+\frac{1}{2}}^{n+\frac{1}{2}} - q_i^{n+\frac{1}{2}}) \quad (17)$$

where h' is the approximate numerical derivative of the bed elevation h . According to Nessyahu and Tadmor [1990], this term is calculated using a limiter in order to ensure that the scheme is *Total Variation Diminishing* (TVD), thus avoiding spurious oscillations of the solution. A β -limiter has been used, as follows

$$h_i' = MM \left[\beta(h_i - h_{i-1}), \frac{1}{2}(h_{i+1} - h_{i-1}), \beta(h_{i+1} - h_i) \right]$$

where β is the limiting parameter and MM , the function MinMod defined by

$$MM\{v_1, v_2, \dots\} = \begin{cases} \min_k \{v_k\} & v_k > 0 \forall k, \\ \max_k \{v_k\} & v_k < 0 \forall k, \\ 0 & \text{otherwise} \end{cases}$$

[19] This scheme allows a value for β up to 4, which is the value used in the morphological module as it led to the less numerical diffusion. More information about this scheme are available in the work of Nessyahu and Tadmor [1990] and its two-dimensional extension can be found in the work of Jiang and Tadmor [1998].

[20] NOCS have already been used for morphological modeling by Callaghan et al. [2006]. Although their sediment flux formulation was nonlinear ($q \sim h^\beta$, $\beta > 1$) it remained an explicit function of the bed form h . In Dune2D, the flux calculations involve both the hydrodynamic and the sediment modules. Thus the calculation of a predicted value for q at step $n + 1/2$ would imply a modification of the code's structure and would also be very expensive in time (about double the numerical cost). In order to avoid this difficulty and to ensure a portability of the morphology module, the predictor step (equation (16)) was replaced by assuming that the sediment flux variations only result from the bed variation, that is to say

$$\frac{\partial q}{\partial x} \approx \frac{\partial q}{\partial h} \frac{\partial h}{\partial x} \quad (18)$$

which gives the nonconservative form of the sediment conservation equation (14) given by

$$\frac{\partial h}{\partial t} + a \frac{\partial h}{\partial x} = 0 \quad (19)$$

where a is the bed celerity, $a \approx \partial q/\partial h$. Consequently, the predictor step (16) was replaced by

$$q_i^{n+\frac{1}{2}} \equiv q\left(t_n + \frac{\Delta t}{2}, x_i\right) = q\left(t_n, x_i - \frac{a\Delta t}{2}\right) \quad (20)$$

[21] Before the morphological calculation, the local bed celerity, a , is calculated locally on the staggered bed grid using a first-degree estimation

$$a_i = \frac{2(q_{i+1} - q_i)}{h_{i+1} - h_{i-1}} \quad \text{if } h_{i+1} \neq h_{i-1} \quad (21)$$

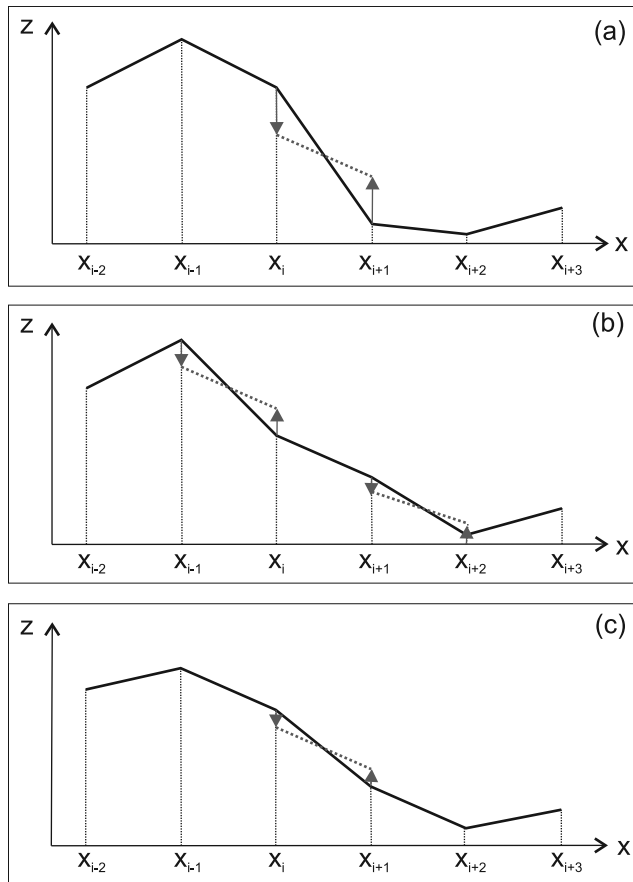


Figure 3. Two iterations of the avalanche algorithm; (a) initial bed form, (b) first iteration, (c) second iteration. Slopes steeper than the angle of stability limit are corrected resulting in a sediment transfer from the crest to the trough. The solid lines represent the bed form at each iteration and the dashed lines represent the angle of repose of sediment.

[22] When $h_{i+1} \simeq h_{i-1}$, that is when the bed form is nearly flat or near a slope inversion (at the ripple crest or trough), a_i is estimated using a third order polynomial estimation $a_i = P^3(x_i)$. The coefficients of P^3 are calculated using two other nodes on each side of the critical nodes: a_{i-2} , a_{i-1} , a_{i+1} , a_{i+2} .

[23] It must be noted that the nonconservative form of the equation is not resolved, only a local estimation of the bed celerity is used. This method can also be replaced by an extrapolation of q at step $n + 1/2$, using q at steps n and $n - 1$ *Marieu* [2007].

[24] The staggered NOCS described above gives the bed elevation at location $i + \frac{1}{2}$. The implementation of the nonstaggered version of NOCS would be simpler. It is the direct extension of the nonstaggered Lax–Friedrich scheme, which calculates the bed elevation at the location $i + 1$ directly, but suffers from significant numerical diffusion. The staggered NOCS has been used in this effort and, in order to avoid an interpolation of the calculated bed height, the scheme (NTCorrector) is performed twice with a half time step $\frac{\Delta t}{2}$ instead of Δt . This implies the estimation of $q^{n+\frac{1}{4}}$ and $q^{n+\frac{3}{4}}$ instead of the estimation of $q^{n+\frac{1}{2}}$ and this is done using the same method as equation (20). A new

calculation of the entire computational grid is performed at each morphological time step. The morphological time step is bounded by numerical diffusion at the upper limit and by the scheme's Courant Friedrichs Lewy (CFL) condition at the lower limit, which imposes $a_i \Delta t / \Delta x < 1$, $\forall i$.

[25] The performance of classical NOCS has already been tested by *Callaghan et al.* [2006] and a simple advection test has been performed by *Marieu* [2007] to observe the behavior of the modified scheme, using the approximation given by equation (18). The modified NOCS performs well to capture the shock location, and a comparison with the original NOCS shows that the scheme modification does not have an influence on the results.

2.5. Avalanching

[26] By not including avalanches that occur at the crest of vortex ripples, a simulated sand ripple could become abnormally steep, leading to nonphysical slopes that exceed the angle of repose of sediment. In natural environments, when the slope is too steep, an avalanche occurs and the sediment is evenly distributed downhill over the slope. In order to simulate the high flux present in avalanches, *Andersen* [1999] recommended fixing the Shields parameter, θ , equal to a downslope fixed value, $\theta = 2$. This method induces large discontinuities in the flux function and the fixed value may be too arbitrary. Consequently, in this effort, a distinct avalanching algorithm has been developed that is performed after each morphological calculation. Figure 3 shows an example of the algorithm. The grid cells where the local slope is steeper than the angle of stability limit are corrected to the sediment angle of repose. The correction is done by changing the two nodes of the cell in such a way that the bed volume is kept constant. This requires a slope change on the neighboring cells and the algorithm is iterated until convergence is achieved. The angle of repose of sediment, ϕ , has been fixed and the angle of stability limit is chosen to be $\phi_l = \phi + 1^\circ$ according to *Courrech du Pont et al.* [2003]. This technique assumes the avalanches are instantaneous with respect to the flow. Moreover, *Doppler* [2005] showed that the angle of stability limit and the angle of repose of sediment depend on the local bed shear stress. However, no observations exist to empirically formulate the dependency, therefore following *Andersen* [1999] ϕ is set to 33° in this effort. This algorithm is not confined to vortex ripples and could be applied to other sedimentary simulations.

3. Results

3.1. Development From a Flat Bed

[27] In the following sections, the morphologic evolution of a rippled bed in response to a single set of hydrodynamic forcing is examined. The seabed is composed of 0.3 mm diameter quartz grained sand ($\rho_s/\rho = 2.65$). The hydrodynamic forcing is sinusoidal with a wave amplitude of $A_0 = 0.25$ m, and period of $T = 6$ s, yielding an excursion velocity amplitude of $U_0 = 0.26$ m/s. Similar hydrodynamic conditions would be expected to be observed within the shoaling zone of intermediate water depths (e.g. a 1 m wave height in 12 m water depth). These conditions were chosen such that the ripple characteristics would be expected to be contained purely within the orbital ripple

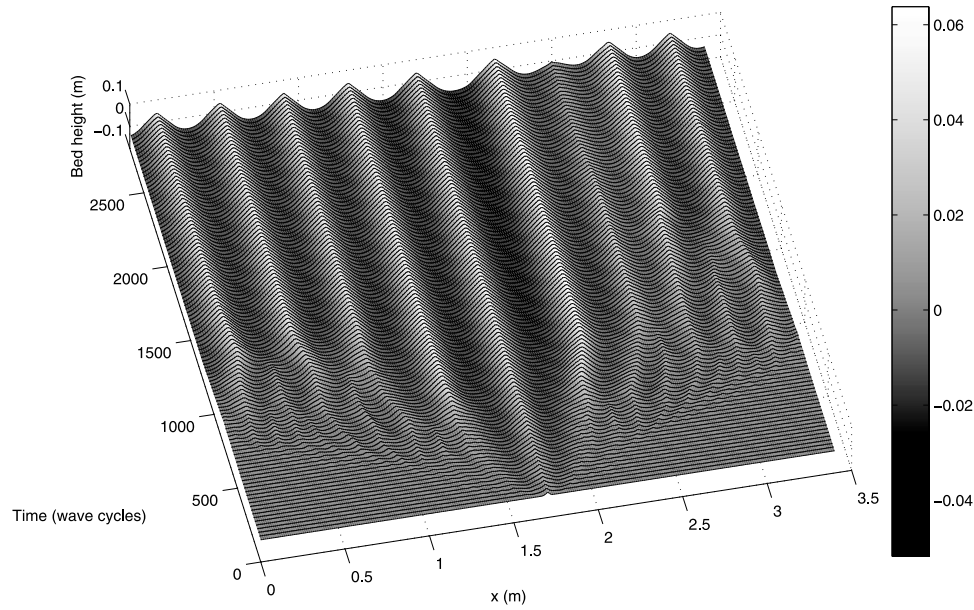


Figure 4. Time evolution of a flat bed locally perturbed by a Gaussian hump; $U_0 = 0.26$ m/s, $T = 6$ s, $d_{50} = 0.3$ mm, $N_x = 900$. The bed form is plotted every 25 wave cycles.

regime according to *Clifton and Dingler* [1984]. The wave mobility number defined by $\Psi = U_0^2/(s-1)gd_{50}$, and the maximum Shields number, θ' , are both low, $\Psi \simeq 14$ and $\theta' \simeq 0.1$. Following the guidelines of *Nielsen* [1992] for low Shields numbers, the bed load formulation of Meyer-Peter and Müller (BedLoadMP) has been employed. The suspended load is small (20% of the total load) relative to the bed load so the formation of ripples is primarily due to bed load transport in this case. Initially, a simulation over a large domain has been performed, in order to limit the influence of the periodic boundary condition on the ripple size. The mean ripple wavelength observed when the bed form reaches a stable form will be used to perform lower cost simulations over smaller domains, containing one or two ripples.

[28] Figure 4 shows the result of the simulation over a large domain of length 3.4 m. 900 horizontal grid cells, N_x , are used for this simulation, and 2000 time steps per wave period ($\Delta t_{hydro} = 3$ ms) are necessary for the convergence of the hydrodynamic module. The morphological calculation and the grid update are done every 10 time steps ($\Delta t = 30$ ms). The initial bed is flat with an initial perturbation supplied by a Gaussian hump at $x = 1.7$ m. The sand bed converges to its quasistable geometry composed of 9 ripples at 1500 wave cycles. At roughly 1500 wave cycles, the 7th ripple slowly decreases in amplitude. In this simulation, there are between 9 ripples (prior to 1500 wave cycles) and 8 ripples (following 1500 wave cycles) which would result in equilibrium wavelengths of 0.425 m and 0.378 m. The wavelength predicted by the orbital law of *Wiberg and Harris* [1994] is $\lambda_r = 1.3 \times A_0 = 0.325$ m, and the empirical relationship of *Nielsen* [1981] for regular waves predicts $\lambda_r = A_0 (2.2 - 0.345 \Psi^{0.34}) = 0.34$ m for $2 < \Psi < 230$. The simulated ripple wavelength is larger than these values but is in better agreement with the field observations of *Traykovski et al.* [1999] and *Ardhuin et al.* [2002]. According to *Traykovski et al.* [1999], the expected wavelength is $\lambda_r = 1.52 A_0 = 0.38$ m, which is very close

to the result obtained with this simulation. The hydrodynamic forcing can be characterized by the dimensionless wave amplitude, A_0/d_{50} , and the period parameter, $\chi = d_{50}/(s-1)gT^2$. According to *Mogridge et al.* [1994], smaller values of χ lead to larger orbital ripples for a fixed value of A_0/d_{50} . In the present simulation, $A_0/d_{50} = 833$ and $\chi = 5.1 \cdot 10^{-7}$, which are more representative of field measurements than flume experiments and allow large orbital ripples [*Mogridge et al.*, 1994; *Traykovski et al.*, 1999].

[29] At saturation, the simulated ripples shape consists of parabolic troughs with triangular crests, the slope near the crests being limited by the crest avalanching. This is consistent with the findings of *Stegner and Wesfreid* [1999], and *Testik et al.* [2006] but the ripple steepness found in this simulation is large: $\eta_r/\lambda_r = 0.228$. This value is in the range of observed ripples [*van Rijn*, 1993] but many studies reported a smaller steepness, in particular *Traykovski et al.* [1999] and *Traykovski* [2007] reported a steepness of 0.17 for their observed orbital ripples, whereas the ripple wavelength obtained in this simulation seems to fit their empirical law. However, in this study the angle of repose is 33° , which could explain why ripples steepness is higher. For example, *Testik et al.* [2006] measured a steepness of 0.22 on asymmetric ripples, with a similar angle of repose (32°).

[30] The initial perturbation grows quickly, its crest moving back and forth by roughly 1 cm at each wave period. Figure 5 shows the evolution of the maximum bed height and the surface elevation standard deviation. In the first 1000 wave cycles, the maximum ripple height grows linearly at $4.6 \cdot 10^{-5}$ m/wave cycle, then the entire bed reaches saturation, at roughly 1500 wave cycles. From laboratory observations, *Voropayev et al.*, 1999 developed an empirical model to predict the ripple growth duration. They give a characteristic timescale, $t^* = c/\omega_0 \Psi^{1/2}$, with the empirical constant, $c = 2500$, derived from their experimen-

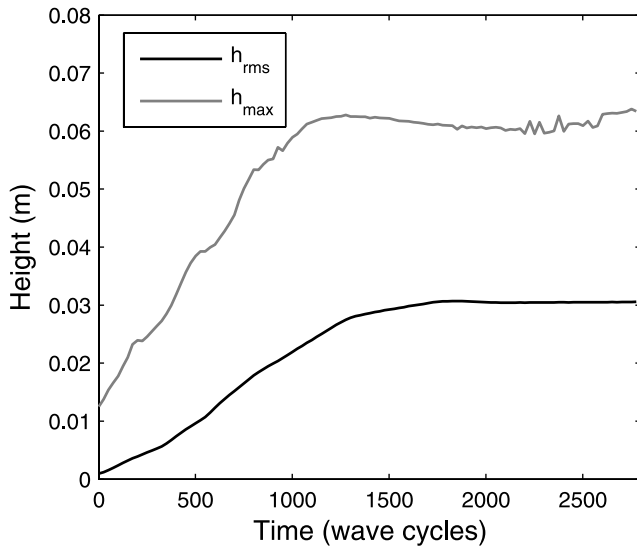


Figure 5. Maximum bed height h_{\max} and standard deviation of the bed height h_{rms} during the evolution of a flat bed locally perturbed by a Gaussian hump; $U_0 = 0.26$ m/s, $T = 6$ s, $d_{50} = 0.3$ mm, $Nx = 900$.

tal data. The ripple growth duration should range between $2t^*$ and $3t^*$. The simulated hydrodynamic conditions of the present study would yield $t^* = 640$ s with a ripple growth duration from 213 to 320 wave cycles. In this case, the growth duration is much longer (1500 wave cycles) because there is a single initial perturbation in the middle of the domain, and that takes time for its propagation on the entire domain. In an experimental environment, the bed has many local perturbations that are likely to grow. A simulation on a smaller domain containing one ripple, $L = 0.378$ m, gave a growth duration of 225 wave cycles, which is in agreement with the Voropayev *et al.* [1999] relationship. An experiment by Stegner and Wesfreid [1999] shows a ripple growth from a flat bed, for a similar mobility number ($\Psi = 13.7$). In this experiment, the time to saturation is of the same order of magnitude (≈ 1800 s) than in the simulation, starting from the instant when the bed is perturbed by rolling-grain ripples.

[31] There are a variety of mechanisms which rule the equilibrium of established ripples when saturation is reached. These mechanisms can be separated into production and damping processes. In equation (17), the term $-\Delta t / \Delta x (q_{i+1}^{n+1/2} - q_i^{n+1/2})$ represents a production term when it is positive and a damping term when it is negative. Numerical diffusion and local avalanches both contribute to the damping processes. The main difference between these terms is that numerical diffusion depends on the slope gradient whereas the avalanche condition depends directly on the slope value. The equilibrium of the bed is reached when the local avalanching balances the production term. This result is consistent with the ripple equilibrium theory of Andersen *et al.* [2001].

[32] The influence of the computational grid on the hydrodynamics and bed shear stress has been examined by Andersen [1999] above a theoretical vortex ripple and by Chang and Hanes [2004] above gently sloped long wave ripples. Andersen [1999] found that the criterion $\Delta x / A_0 <$

0.012 was required to avoid instabilities near the crest. Here we continue with those efforts and examine the model sensitivity to the morphological time step and the bed grid refinement. The bed evolution has been simulated for 8 horizontal grid resolutions, $Nx = 40, 60, 80, 100, 120, 140, 160, 180$, and three morphological time steps, for a length $L = 0.378$ m allowing the development of one ripple. The bed energy is defined as the standard deviation of the bed height. Figure 6 shows the sensitivity of the time to saturation, t^{sat} , and the bed energy at saturation, $h_{\text{rms}}^{\text{sat}}$. The bed energy at equilibrium is defined as the bed energy averaged on the 100 last wave cycles of the simulation and the time to saturation is defined as the number of wave cycles necessary for the bed energy to reach 95% of the bed energy at equilibrium. When the grid is too coarse or the time step is too small, the numerical diffusion of the morphological scheme becomes high relative to the sediment fluxes and the initial bed evolves to a flat bed form ($h_{\text{rms}}^{\text{sat}} = 0$). If the grid is too refined or if the time step is too large, the CFL condition is not satisfied and the resulting bed is unstable, it happens when $Nx = 180$ if $\Delta t_{\text{morph}} = 5 \Delta t$, when $Nx \geq 140$ if $\Delta t_{\text{morph}} = 10 \Delta t$, and when $Nx \geq 120$ if $\Delta t_{\text{morph}} = 20 \Delta t$. There is a strong sensitivity of the growth rate to the resolution, as the saturation time decreases with increasing grid refinement. Not surprisingly, there is a lower sensitivity to the morphologic time step because the numerical diffusion is a square function of the grid spacing, but only a linear function of the time step. For the cases where the CFL condition is satisfied, the bed energy at saturation shows only 7% variability. This small variability is mainly due to the avalanche condition, which limits the ripple height whatever the time step or the grid spacing are. However, the avalanche condition has less influence during the ripple growth, which explains why the time to saturation is more influenced by the grid spacing and time step than the bed energy at saturation. The Morphologic sensitivity to bed load formulation and slope correction is shown in

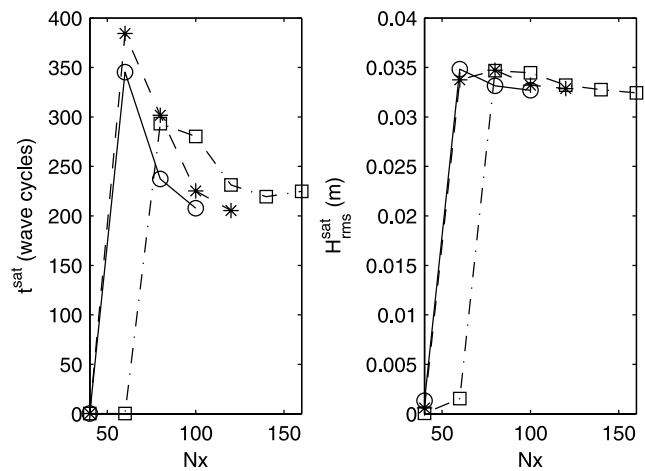


Figure 6. Influence of grid and morphological time step on the time to saturation (left) and on the bed energy at saturation (right). The squares represent $\Delta t_{\text{morph}} = 5 \Delta t$, the stars represent $\Delta t_{\text{morph}} = 10 \Delta t$, and the circles represent $\Delta t_{\text{morph}} = 20 \Delta t$. The results from unstable simulations are not shown (e.g., $Nx = 180$ if $\Delta t_{\text{morph}} = 5$, $Nx \geq 140$ if $\Delta t_{\text{morph}} = 10$, and $Nx \geq 120$ if $\Delta t_{\text{morph}} = 20$).

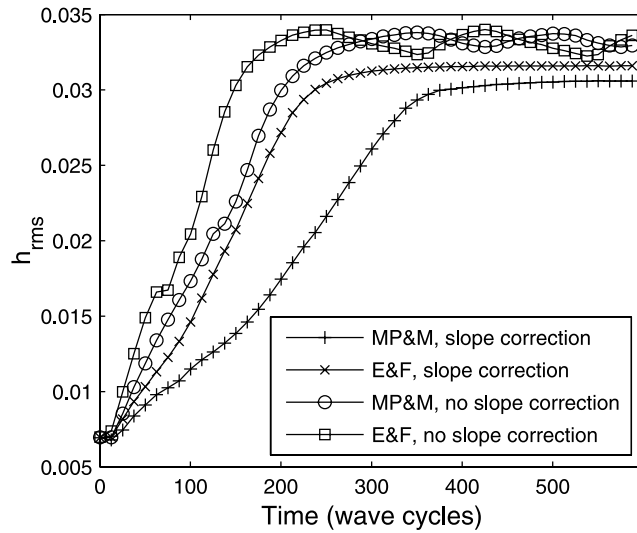


Figure 7. Temporal evolution of the bed form height standard deviation h_{rms} for four flux formulations considering the bed load models of Meyer-Peter and Müller (MP and M) or Engelund and Fredsøe (E and F) both with or without slope correction.

Figure 7. In all cases the hydrodynamic forcing was uniform. Both the bed load formulation and the slope correction have a significant influence on both the growth rate, and the bed energy at equilibrium. The slope correction applied to the critical Shields parameter tends to reduce the flux directed from the ripple trough toward the ripple crest and this leads to slightly smaller bed forms. Of the four simulations shown in Figure 7, the slope-corrected Meyer-Peter and Müller formulation is the most consistent with the characteristic timescale given by the empirical relation of Voropayev *et al.* [1999] for these forcing conditions.

3.2. Ripple Evolution Processes

[33] An example of ripple creations, mergers and annihilations is given in Figure 8. For this simulation, the domain length is 0.756 m, therefore when saturation is reached, the domain is expected to be covered by two ripples. Figure 9 shows the flow field and suspended sediment over the initial bed form, in the vicinity of the perturbation. The velocity vectors, the concentration of sediment, the horizontal flux of sediment and the flux gradient, given by $-(q_{i+1} - q_i)/(x_{i+1} - x_i)$, are shown at the peak free stream wave velocity ($t = T/4$). The concentration of sediment (upper panel) highlights the influence of the recirculation bubble, and the opposite of the flux gradient (lower panel) shows the erosion and deposition zones. Two strong variations are visible in the flux gradient. One results from the contrast between the flow acceleration on the left slope of the ripple and deceleration at the ripple crest (at $x = 0.37$ m). Sediment is eroded from the left slope of the ripple and deposited on the ripple crest, resulting in a rightward crest displacement. The other strong variation is situated at the stagnation point at $x = 0.41$ m, where the leftward flux induced by the end of the recirculation bubble generates an erosion zone which is responsible for the ripple development and propagation.

[34] Figures 4 and 8 show small perturbations that are created on each side of the initial perturbation. Figure 10 shows the evolution of the flux gradient averaged over one wave period at three different wave cycles. The erosion zones situated on each side of the initial perturbation increase the ripple steepness but are filled by the crest avalanching. The second erosion zones are not filled by the crest avalanching and they are responsible for the formation of two other perturbations on each side of the first one. The spatial scale of the erosion zones are limited by the amplitude of the vortex during one wave period. The new created depressions (at $t = 107$) imply the creation of new vortices that will lead to new zones of convergence and initiate new perturbations on the bed form. If the first perturbation is small, the secondary perturbations are very

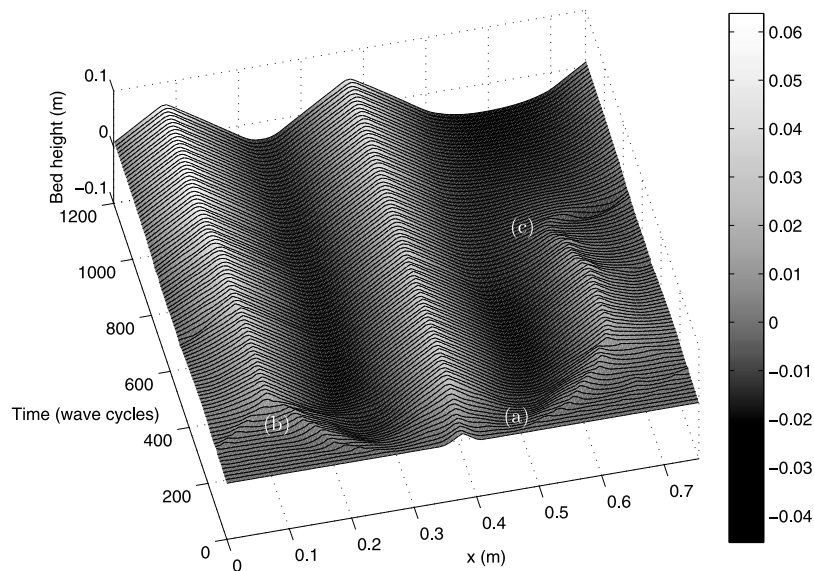


Figure 8. Ripple growth and creation (a), ripple merging (b), and ripple annihilation (c) during a sandy bed evolution; $U_0 = 0.26$ m/s, $T = 6$ s, $d_{50} = 0.3$ mm, $N_x = 200$.

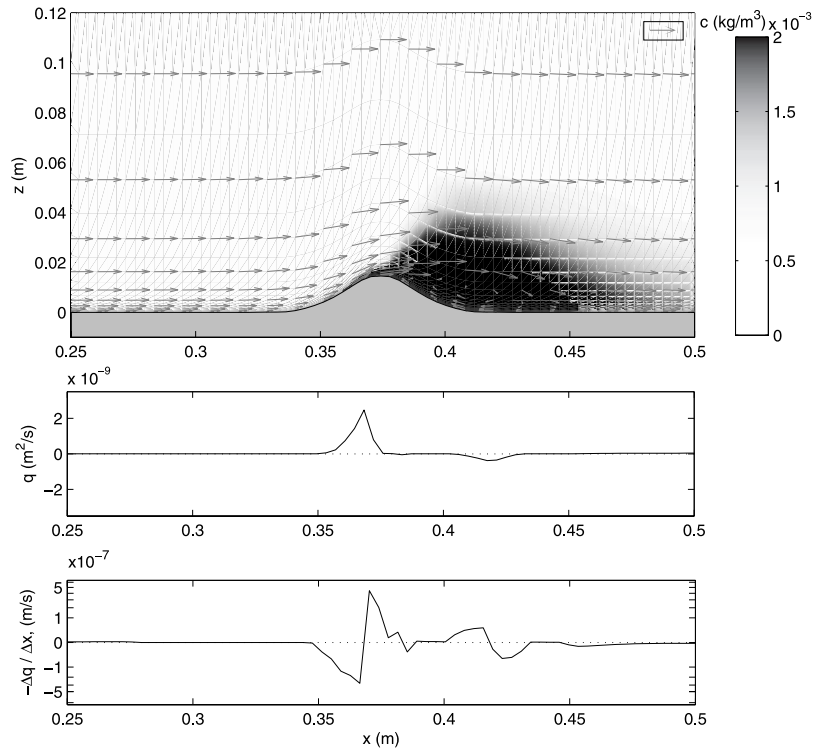


Figure 9. Velocity field and concentration (top), horizontal flux of sediment (center), and opposite of the flux gradient (bottom) over the initial bed form at $t = T/4$ zoomed on the perturbation. A 0.25 m/s scale vector is shown in the top right corner at the top. The flux gradient is plotted on a nonlinear axis for a better visualization.

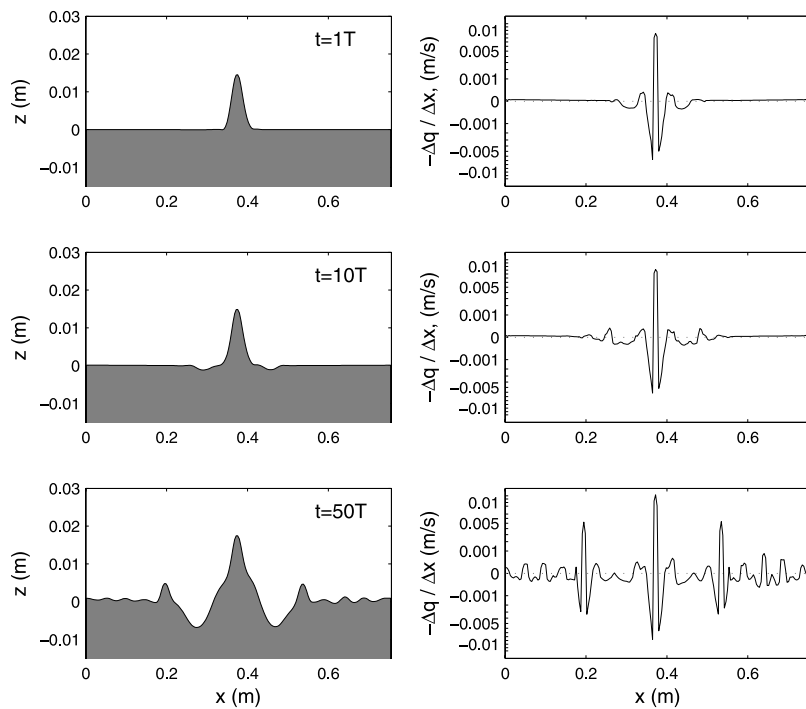


Figure 10. Evolution of the bed form (left) and erosion–deposition rate averaged over one wave period (right) during ripple creation at $t = T$, $t = 10T$, $t = 50T$.

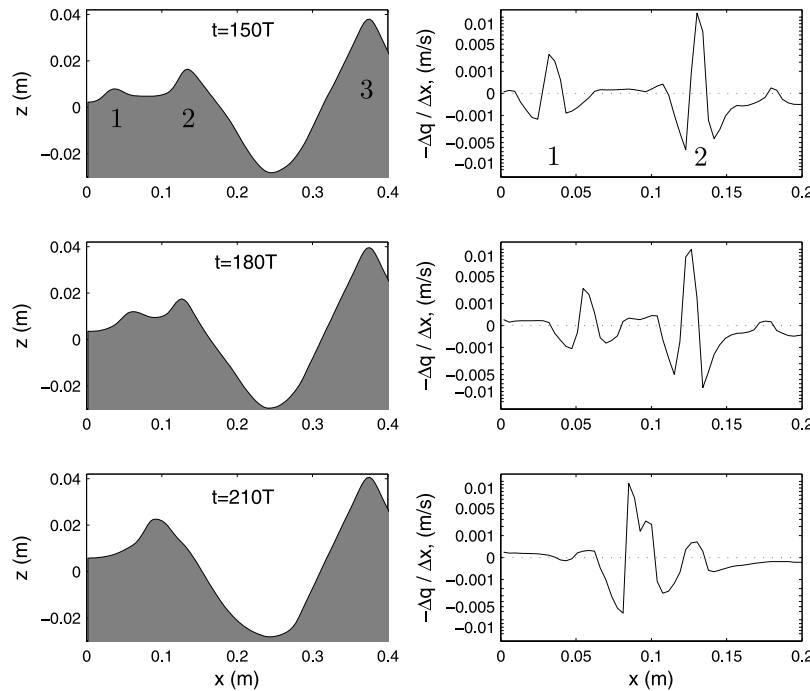


Figure 11. Evolution of the bed form (left) and the flux gradient averaged over one wave period (right) during the merging of ripple 1 and ripple 2 at $t = 150T$, $t = 180T$, $t = 210T$.

close to the first one, but as the first perturbation grows, the recirculation bubbles are larger, driving the secondary perturbations to migrate away from the initial perturbation. The phenomenon is repeated until the entire domain is covered by ripples and saturation is reached. Saturation occurs when each side of the ripple reaches the angle of repose, then avalanches will prevent further evolution. This process underlines the importance of the vorticity calculations. As shown in *Chang and Scotti* [2004], RANS models with $k-\omega$ closure schemes can over predict the extent of the recirculation bubbles, suggesting that a large-eddy simulation may predict smaller ripple wavelengths.

[35] Figure 11 shows the evolution of the bed form and the flux gradient during the merging of ripples 1 and 2 which occurs between 150 and 210 wave cycles. The initial perturbation 3 has grown and the vortices that it creates are getting larger. The vortex generated by ripple 3 on its left side is larger than the one generated by ripple 2 on its right side. Thus ripple 2 is displaced to the left. The asymmetry of ripple 2 affects the generated vortices. The vortex generated on the left of the ripple is much smaller than the one on the right, resulting in a deposition of sediment between ripple 1 and ripple 2. This can be observed on the right panels, which show the flux gradient. Ripple 1 is supplied in sediment on its right side and displaces to the right while ripples 1 and 2 merge.

[36] Figure 12 shows the bed form evolution and the sediment flux averaged over a wave cycle during the ripple annihilation shown in Figure 8c. The domain length has been chosen in such a way that two orbital ripples will exist at saturation. The initial perturbation is situated on the middle of the domain, leading to the development of three ripples. One of them is annihilated at $t = 800T$, allowing the sand bed to converge to the saturated bed form composed of

two orbital ripples. The ripple situated on the right of the domain is slightly smaller than the two other ripples and generates two smaller vortices. It induces a negative mean flux on the left slope of the ripple and positive flux on the right slope. This leads to a lack of sediment on the crest of the ripple which vanishes while the others two grow slightly. Following the annihilation, the two remaining ripples diverge from one other slowly. When the equilibrium size of the ripples is reached, both ripples stabilize as the generated vortices reach their maximum size.

[37] The role of suspension in ripple development can be significant. Table 1 shows some results from the comparison between the simulation presented Figure 8 and the same simulation without suspension. The suspended load is small compared to the bed load during the ripple evolution, therefore most of the total flux is due to the bed load, and the suspended load has only a small influence on the bed form evolution. The suspended load weakens the bed load fluxes from 0% to 20%, therefore ripple development is accelerated when suspension is switched off. At saturation, the final bed is composed of two ripples in both cases, the ripples height being slightly higher when the suspension is deactivated. For these moderate hydrodynamic conditions, the suspended sediment is not able to jump the ripple crests, trapped in the ripple troughs by the vortices. In the end, suspension does not have a particular influence on ripple evolution processes with these moderate flow conditions, apart on the amount of total sediment flux. This might not be the case for higher energy flows for which the contribution of suspended load must be studied carefully.

3.3. Evolution From Random Bed Forms

[38] Other simulations have been done with random initial bed forms. Figure 13 shows the bed form evolution on a large domain, starting from a random bed with large

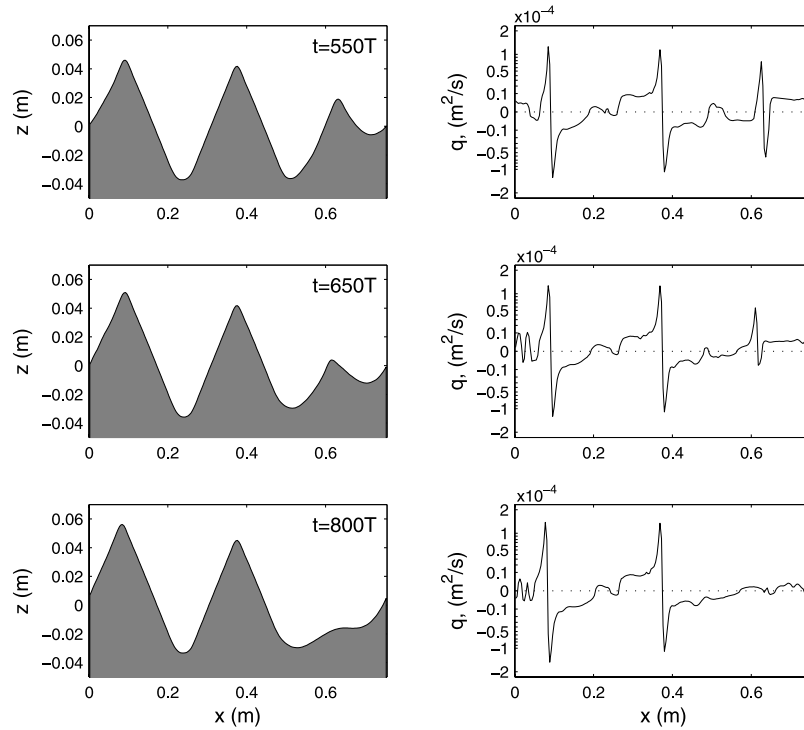


Figure 12. Evolution of the bed form (left) and the total flux of sediment averaged over one wave period (right) during ripple annihilation at $t = 550T$, $t = 650T$, $t = 800T$.

oscillations. In this case, the initial bed represents a relic bed form which is more energetic than the bed form obtained at equilibrium, Figure 4. The bed form tends to reach an equilibrium state that is close to the one obtained at the end of the evolution from a quasiflat bed. Figure 14 shows the evolution of the bed form spectrum, which allows a better understanding of the evolution stages. Until 500 wave cycles, small ripples (λ_r of approximately 0.25 m) are developing over the existing large sand waves which do not immediately disappear, which is consistent with the field observations of *Traykovski et al.* [1999] and *Traykovski* [2007]. From 500 to 800 wave cycles, these small ripples are growing and merging to form larger ripples that have the equilibrium wavelength (of approximately 0.4 m), while the large oscillations lose energy. At 800 wave cycles, the bed form is close to the final bed form, however it is still transferred afterward from the large oscillations to the equilibrium wavelength. This process is slow as the transport rate for ripples near equilibrium is small, and the bed form has to reorganize in order to allow the sediment transfer from the higher to the lower areas.

[39] Figure 15 shows the evolution of the standard deviation of the bed height during the simulation. The ripple evolution can be separated in three stages: organization, growth, and saturation. In the case starting from a quasiflat bed, the initial energy of the bed is quasinnul, therefore the evolution begins directly with the growth stage until saturation is reached. An organization stage is necessary when the sandy bed is in equilibrium with a previous hydrodynamic forcing and has to adapt to the new hydrodynamics. On Figure 15, the organization stages are represented with decreasing of the bed energy. They occur during the creation of small ripples over the large oscillations, from

0 to 500 wave cycles, and during the transfer of energy from higher to lower areas, from 1000 to 2500 wave cycles. The organization stages can be slow compared to the growth stages and depend strongly on the bed history. In other studies, *Traykovski* [2007] and *Testik et al.* [2005] measured a quick adaptation of the bed form, even when the hydrodynamics is reduced from a large wave forcing to a moderate wave forcing. However, it is not the same case in this simulation, as the initial bed is not covered by saturated ripples. The gentle sloping initial bed form does not generate as large vortices as a full rippled bed which would induce ripple splitting [*Hansen et al.*, 2001b; *Stegner and Wesfreid*, 1999; *Testik et al.*, 2005], and in this simulation the bed form has to develop from small local perturbations.

[40] Figure 16 shows 10 simulations that have been done on a smaller domain, $L = 0.378$ m, starting from random bed forms or organized bed forms (2, 3, or 6 regular orbital ripples with parabolic shapes). At saturation, simulations

Table 1. Comparison Between Results Obtained With or Without the Suspended Load Activation on the Simulation (Figure 8)^a

	Suspension Activated	Suspension Deactivated
Number of ripples at saturation	2	2
h_{rms}^{sat} , m	0.035	0.037
t_{rms}^{sat} wave cycles	944	680
$\bar{q}_s^{init}/\bar{q}_s^{init}$, $m^2/s \times 10^{-4}$	0.04/0.49	0.0/0.45
$\bar{q}_s^{sat}/\bar{q}_s^{sat}$, $m^2/s \times 10^{-4}$	0.16/0.74	0.0/1.08

^a \bar{q}_s^{init} and \bar{q}_s^{init} are respectively the mean suspended load and the mean total flux over the initial perturbation. \bar{q}_s^{init} and \bar{q}_s^{init} are respectively the mean suspended load and the mean total flux over the final bed.

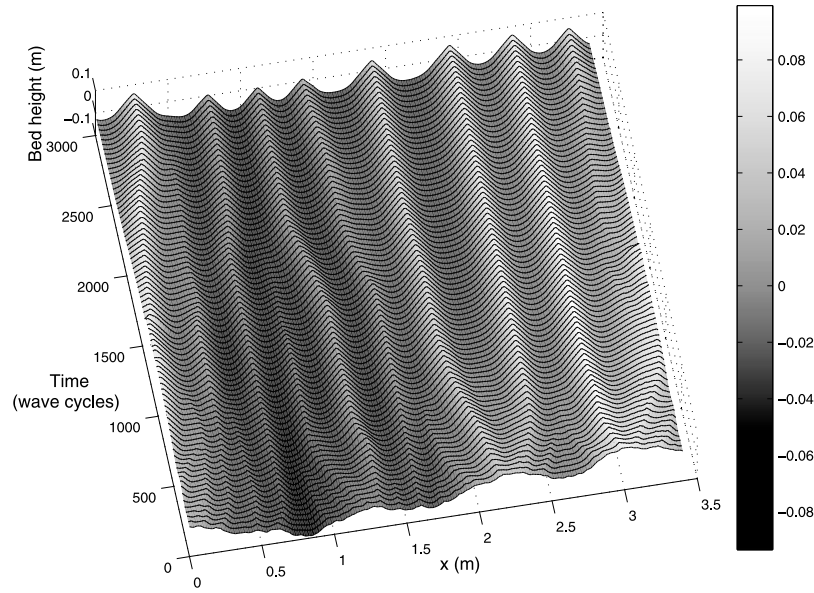


Figure 13. Time evolution of a randomly rippled bed; $U_0 = 0.26$ m/s, $T = 6$ s, $d_{50} = 0.3$ mm, $Nx = 900$.

generally evolve into a final bed form made of 1 regular vortex ripple. The exception is case (c) for which the bed form is blocked with 2 small ripples, due to the symmetry of the system. In a natural environment, small variations in the wave intensity, the wave direction, or the sediment distribution can break this quasistable stage. Moreover, the development of three-dimensional ripples may facilitate the bed form evolution [Traykovski *et al.*, 1999]. Saturation times vary and are dependent on whether the initial bed form is close to the equilibrium bed form. For example, case (e) reaches saturation very quickly because the initial bed form has already a single large ripple. On the contrary, case (f) takes a long time to reach saturation. The bed form initially evolves to 3 ripples, then 2 of the 3 ripples are annihilated successively. These results show that the bed history has a strong influence on the time of evolution, even if the bed tends to evolve to the same equilibrium form. In further studies, the wave conditions around the stability balloon evoked by Hansen *et al.* [2001a] could be explored

with the model in order to study how equilibrium ripples adapt to a different forcing. If ripple splitting might be successfully simulated with the model, as suggested by the ripple creation processes, pearling and even bulging instabilities would necessitate a three-dimensional model.

3.4. Dissipation of Wave Energy

[41] The total wave energy dissipation averaged on the entire domain and for each wave period, D_E , has been calculated during bed form evolutions. It allows for the calculation of the energy dissipation factor, f_e , averaged over each wave period. f_e is obtained from the formulation of Jonsson [1966],

$$f_e = \frac{3\pi}{2} \frac{D_E}{\rho U_0^3}. \quad (22)$$

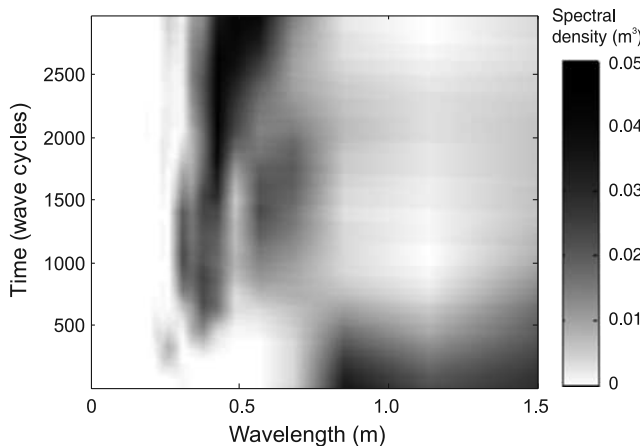


Figure 14. Evolution of the bottom elevation spectral density starting from a random rippled bed; $U_0 = 0.26$ m/s, $T = 6$ s, $d_{50} = 0.3$ mm, $Nx = 900$.

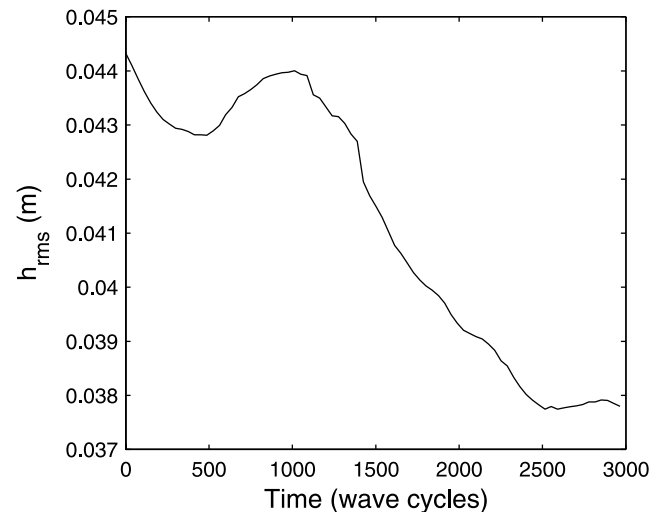


Figure 15. Standard deviation of the bed height h_{rms} starting from a random rippled bed; $U_0 = 0.26$ m/s, $T = 6$ s, $d_{50} = 0.3$ mm, $Nx = 900$.

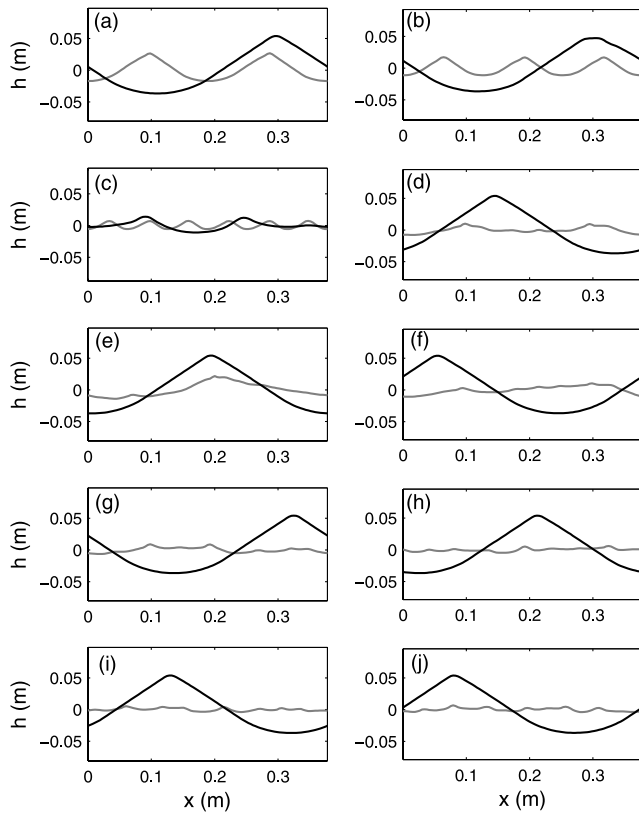


Figure 16. Initial and final bed forms for 10 simulations on a small domain ($Nx = 100$). Gray lines represent the initial bed forms, and black lines represent the final bed forms. Initial domain are either organized with (a) two ripples, (b) three ripples, and (c) six ripples, or randomly generated (d), (e), (f), (g), (h), (i), and (j).

[42] On a flat bed, the wave energy dissipation factor is 0.0098 and corresponds to the value calculated by the corrected Swart's formula (e.g. *Nielsen* [1992]) on a rough bed, for $d_{90} = 0.3$ mm and $A_0 = 0.25$ m,

$$f_e = \exp \left[5.5 \left(\frac{2d_{90}}{A_0} \right)^{0.2} - 6.3 \right] = 0.0095. \quad (23)$$

[43] The wave energy dissipation factor has been calculated during the bed form evolution. Figure 17 shows the evolution of the energy dissipation factor during the bed evolution starting both from a quasiflat bed (e.g. Figure 4) and from a random “relic” bed (e.g. Figure 13). For the quasiflat bed case, the dissipation factor increases with increasing bed roughness, in the same time that the bed energy grows. The energy dissipation factor for the equilibrium profile is $f_e = 0.25$, which is about 25 times the dissipation factor on a flat bed with the same hydrodynamic forcing. This value is of the order of magnitude of the bottom friction obtained with *Grant and Madsen* [1986] model but is twice larger than the value obtained with the three-layer model developed by *Styles and Glenn* [2000]. However, the last is accurate for high near-bed velocities, where large ripples are washed out, and the orbital ripples

obtained with the simulation seem too high for the three-layer model to be valid.

[44] Despite the height of the initial bed form, the gentle slope of the initial long ripples leads to a low wave energy dissipation. Until 1000 wave cycles, the f_e for the random bed case increases at the same rate than on the initial quasiflat bed. This is due to the development and growth of the orbital ripples on the relic bed form. However, the energy dissipation factor decreases during ripple annihilations. This is particularly visible from about 1400 to 1600 wave cycles, when a large orbital ripple is annihilated (e.g., Figure 13). These ripple annihilations allow the bed to reorganize, then the ripple growth is initiated again, leading to another increase of the wave energy dissipation factor. The 10 simulations that have been done on a smaller domain with random initial bed forms confirmed this result, showing a decrease of the wave energy dissipation during ripple annihilation, and an increase during ripple merging. Ripples organizations lead to a ripple growth, therefore the final wave energy dissipation is higher. In these simulations, the initial bed forms never generate as much energy dissipation as the equilibrium bed form. This is an interesting result for the study of the wave dissipation on relic ripples but it must be further investigated for generalization. The presence of relic gently sloping bed forms will not yield as much dissipation as an equilibrium rippled bed.

[45] The morphology module allows the study of the bed form feedback on the waves that generate it. An important application of the present work is the study of swell dissipation on a continental shelf, in order to provide an understanding of energy dissipation factors included in swell propagation models. The low energy dissipation on relic ripples could explain why *Ardhuin et al.* [2003] had to decrease the energy dissipation factor estimated in laboratory by *Madsen et al.* [1990] when modeling swell propagation across the continental shelf, in order to fit observed wave heights. As the duration of the bed evolution until saturation is very long for low energy flows (nearly five hours for the present simulation), the bed history cannot be

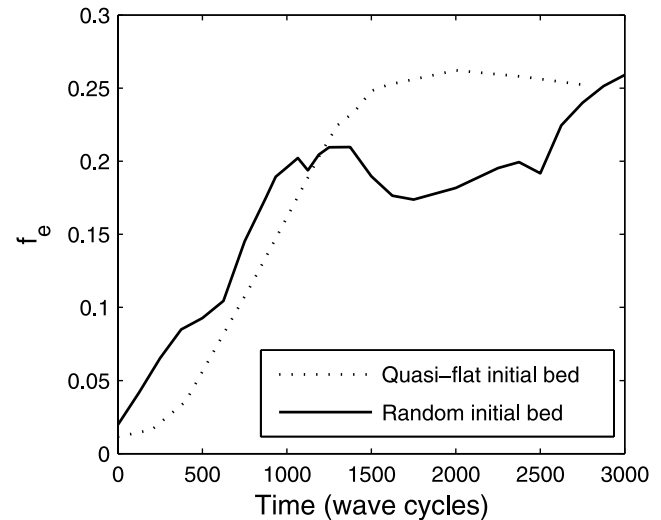


Figure 17. Evolution of the energy dissipation factor f_e starting from quasiflat bed or a random rippled bed; $U_0 = 0.26$ m/s, $T = 6$ s, $d_{50} = 0.3$ mm, $Nx = 900$.

neglected for the estimation of the energy dissipation factor. Of course many other effects such as the three-dimensional nature of the ripple, sediment heterogeneity, wave randomness, and the intergranular interaction also come into play and require further investigation.

4. Conclusions

[46] A new morphological module has been developed and tested for simulations of sandy bed evolution. This method, based on a nonoscillatory central scheme with a local avalanche routine allows the simulation of vortex ripples creation and evolution until reaching an equilibrium state of the sandy bed in response to a regular hydrodynamic forcing. This equilibrium is obtained when the damping processes balance the production processes. The production processes are induced by the vortices whereas the dominant damping process that limits the steepness of ripples is the local avalanche of the crest. The equilibrium between these two phenomena is reached when the avalanches of the ripple slopes balances the sediment flux generated by the vortices.

[47] When simulations are performed from random bed forms, both the bed growth rate and pattern agree with published experimental results. Not surprisingly, when the simulations are initiated from a quasiflat bed form, the growth time is much longer due to the propagation of the initial perturbation on the domain. The growth time is a function of the numerical diffusion and bed load formulation. Therefore the parameters governing the morphological module (Δt , N_x , and fluxes formulations) must be carefully adapted to the studied phenomenon. A comparison with experimental measurements of growth rates can be used as a criterion to calibrate the fluxes formulations. There is evidence to suggest that the slope-corrected formulation of *Meyer-Peter and Müller* [1948] is appropriate for the calculation of bed load transport over ripples, at low stress values.

[48] The application of the morphology module to the evolution of a quasiflat sandy bed allows the local study of the development, merging, and annihilation of ripples. These processes are consequences of the vortices formation, ejection, and advection over individual ripples. The vortices induce sign inversions of the sediment fluxes which create erosion zones and deposition zones, allowing for the creation and development of new ripples. A merging occurs when two ripples are situated between two other ripples that generate vortices of a larger magnitude. In this case, the formers get closer one to the other, and eventually merge. Ripple annihilation occurs when a ripple is situated between two larger ripples which generate larger vortices. These vortices transport sediment away from the ripple crest until the ripple vanishes.

[49] For the case studied, the bed evolution from random initial bed forms shows that the bed tends to evolve to the same final bed form regardless of the initial bed form. However, this evolution is slow once the bed has reached a state close to the final form. In this case, an organization stage occurs where sediment is transferred between ripples. This transfer can last a long time due to the difficulties for sediment to travel above an orbital ripple that has reached a quasiequilibrium. However, in natural environments, ripples

are not confined in boundaries and three dimensional effects can accelerate the bed evolution. It can be supposed that organization stages are easier when the fluxes are dominated by the transport of sediment in suspension.

[50] The morphology module presented here allows the study of the wave energy dissipation above relic sand beds. The first results above random bed forms confirm that the ripple steepness is the main cause of energy dissipation. The bed height is also a factor of dissipation and larger structures induce more energy dissipation than smaller ones, for a given steepness. The study of energy dissipation over moving bed forms is a tool for wave propagation models on continental shelves. The values of f_e obtained here cannot be directly extrapolated to the field, but the present work clearly suggests that bed history cannot be ignored for wave dissipation, even though it is likely less important in three dimensions.

[51] This study has been performed for orbital ripples but more investigations should be done, forcing with other hydrodynamic conditions to understand the physical processes that induce other ripple regimes, such as anorbital ripples. An investigation of various hydrodynamic regimes, using the model, would certainly help to clarify these phenomena. As ripple migration is a significant mode of cross-shore sediment transport in coastal areas, an interesting field for further investigations is the study of migration velocities under wave-current flows, and asymmetric waves. Moreover, the developed morphological module gave good results for the study of ripples but could also be applied to other morphological applications such as nearshore sandbar morphodynamics.

[52] **Acknowledgments.** This research is supported by the French Service Hydrographique et Océanographique de la Marine research contract CA 2003/07/CMO. We are grateful to the Technical University of Denmark who developed the Dune2D model and provided it for this study.

References

- Andersen, K. H. (1999), The dynamics of ripples beneath surface waves and topics in shell models of turbulence, Ph.D. thesis, Det Naturvidenskabelige Fakultet Kbenhavns Universitet. (<http://mail.isva.dtu.dk/~ken/Thesis.html>)
- Andersen, K. H., M.-L. Chabanol, and M. van Hecke (2001), Dynamical models for sand ripples beneath surface waves, *Phys. Rev. E*, **63**(1), 066308, doi:10.1103/PhysRevE.63.066308.
- Ardhuin, F., T. G. Drake, and T. H. C. Herbers (2002), Observations of wave-generated vortex ripples on the North Carolina continental shelf, *J. Geophys. Res.*, **107**(C10), 3143, doi:10.1029/2001JC000986.
- Ardhuin, F., T. H. C. Herbers, P. F. Jessen, and W. C. O'Reilly (2003), Swell transformation across the continental shelf: Part II. Validation of a spectral energy balance equation, *J. Phys. Oceanogr.*, **33**, 1940–1953.
- Bagnold, R. A. (1946), Motion of waves in shallow water, interaction between waves and sand bottoms, *Philos. Trans. R. Soc. London*, **A187**, 1–15.
- Blondeaux, P. (1990), Sand ripples under sea waves: Part 1. Ripple formation, *J. Fluid Mech.*, **218**, 1–17.
- Bradshaw, P., B. E. Launder, and J. L. Lumley (1996), Collaborative testing of turbulence models, *J. Fluids Eng., Trans. ASME*, **118**(2), 243–246.
- Caleffi, V., A. Valiani, and A. Bernini (2006), Fourth-order balanced source term treatment in central weno schemes for shallow water equations, *J. Comput. Phys.*, **218**, 228–245, doi:10.1016/j.jcp.2006.02.001.
- Callaghan, D. P., F. Saint-Cast, P. Nielsen, and T. E. Baldock (2006), Numerical solutions of the sediment conservation law; a review and improved formulation for coastal morphological modelling, *Coastal Eng.*, **53**, 557–571, doi:10.1016/j.coastaleng.2006.03.001.
- Chang, Y. S., and D. M. Hanes (2004), Suspended sediment and hydrodynamics above mildly sloped long wave ripples, *J. Geophys. Res.*, **109**, C07022, doi:10.1029/2003JC001900.
- Chang, Y. S., and A. Scotti (2004), Modeling unsteady turbulent flows over ripples: Reynolds-averaged Navier-Stokes equations (RANS) versus

- large-eddy simulation (LES), *J. Geophys. Res.*, **109**, C09012, doi:10.1029/2003JC002208.
- Clifton, H. E., and J. R. Dinger (1984), Wave-formed structures and paleoenvironmental reconstruction, *Mar. Geol.*, **60**, 165–198.
- Courrech du Pont, S., P. Gondret, B. Perrin, and M. Rabaud (2003), Granular avalanches in fluids, *Phys. Rev. Lett.*, **90**(4), 044301, doi:10.1103/PhysRevLett.90.044301.
- Darwin, G. H. (1883), On the formation of the ripple-mark in sand, *Philos. Trans. R. Soc. London*, **A36**, 18–43.
- Doppler, D. (2005), Stabilité et dynamique de pentes granulaires sous-marines, Ph.D. thesis, Université Paris XI, spécialité Mécanique Physique.
- Engelund, F., and J. Fredsøe (1976), A sediment transport model for straight alluvial channels, *Nord. Hydrol.*, **7**, 293–306.
- Eriksson, L. E. (1982), Generation of boundary-conforming grids around wing-body configurations using transfinite interpolation, *ALAA J.*, **20**, 1313–1320.
- Foster, D. L., S. T. Foster, A. K. Foster, E. B. Fredsøe, and J. Thornton (2001), Model-data comparisons of velocity and suspended sediment in a wave dominated environment, in *Proceedings of the Coastal Dynamics '01*, pp. 751–758, ASCE.
- Fredsøe, J., and R. Deigaard (1992), *Mechanics of coastal sediment transport*, *Advanced Series on Ocean Engineering*, vol. 3, World Scientific Publishing Co. Pte. Ltd.
- Fredsøe, J., and S. Tjerry (2001), Morphological computation of dunes, in *Proceedings of the Symposium on River, Coastal and Estuarine Morphodynamics, Obihiro, Japan*, pp. 225–231.
- Grant, W. D., and O. S. Madsen (1982), Movable bed roughness in unsteady oscillatory flow, *J. Geophys. Res.*, **87**, 469–481.
- Grant, W. D., and O. S. Madsen (1986), The continental-shelf bottom boundary layer, *Annu. Rev. Fluid Mech.*, **18**, 265–305.
- Hansen, J. L., M. van Hecke, C. Ellegaard, K. H. Andersen, T. Bohr, A. Haaning, and T. Sams (2001a), Stability balloon for two-dimensional vortex ripple patterns, *Phys. Rev. Lett.*, **87**(20), 204301, doi:10.1103/PhysRevLett.87.204301.
- Hansen, J. L., M. van Hecke, C. Ellegaard, K. H. Andersen, T. Bohr, and T. Sams (2001b), Pattern formation: Instabilities in sand ripples, *Nature*, **410**, doi:10.1038/35066631.
- Jiang, G.-S., and E. Tadmor (1998), Nonoscillatory central schemes for multidimensional hyperbolic conservation laws, *SIAM J. Sci. Comput.*, **19**(6), 1892–1917.
- Johnson, H. K., and J. A. Zyserman (2002), Controlling spatial oscillations in bed level update schemes, *Coastal Eng.*, **46**(6), 109–126, doi:10.1016/S0378-3839(02)00054-6.
- Jonsson, I. G. (1966), Wave boundary layers and friction factors, in *Proceedings of the 10th International Conference of Coastal Engineering*.
- Leonard, B. P. (1979), A stable and accurate convective modelling procedure based on quadratic upstream interpolation, *Comput. Methods Appl. Mech. Eng.*, **19**, 59–98.
- Leveque, R. J. (2002), *Finite volume methods for hyperbolic problems*, *Cambridge texts in applied mathematics*, vol. 1, Cambridge Univ. Press.
- Li, M., and B. A. O'Connor (2007), Numerical study of sediment transport above rippled beds under the action of combined waves and currents, *Sedimentology*, **54**(6), 1345–1363.
- Liu, X.-D., S. Osher, and T. Chan (1994), Weighted non-oscillatory central scheme, *J. Comput. Phys.*, **115**(1), 200–212.
- Long, W., J. T. Kirby, and Z. Shao (2008), A numerical scheme for morphological bed level calculations, *Coastal Eng.*, **55**(2), 167–180, doi:10.1016/j.coastaleng.2007.09.009.
- Madsen, O. S., P. P. Mathisen, and M. M. Rosengaus (1990), Movable bed friction factors for spectral waves, in *Proc. 22nd Int. Conf. Coast. Eng.*, pp. 420–429, ASCE.
- Marieu, V. (2007), Modélisation de la dynamique des rides sédimentaires générées par les vagues, Ph.D. thesis, Ecole Doctorale Sciences de l'Environnement de l'université Bordeaux 1.
- Meyer-Peter, E., and R. Müller (1948), Formulas for bed-load transport, in *Proceeding of the International Association of Hydraulic Research, 3rd Annual Conference, Stockholm*, pp. 39–64.
- Mogridge, G. R., M. H. Davies, and D. H. Willis (1994), Geometry prediction for wave-generated bedforms, *Coastal Eng.*, **22**(C11), 255–286.
- Natoo, P. (2003), Evaluation of near bed suspension in a wave and current dominated environment, Master's thesis, Ohio State Univ., USA.
- Nessyahu, H., and E. Tadmor (1990), Non-oscillatory central differencing for hyperbolic conservation laws, *J. Comput. Phys.*, **87**(1), 408–463.
- Nielsen, P. (1981), Dynamics and geometry of wave-generated ripples, *J. Geophys. Res.*, **86**(C7), 6467–6472.
- Nielsen, P. (1992), *Coastal bottom boundary layers and sediments transport*, *Advanced Series on Ocean Engineering*, vol. 4, World Scientific Publishing Co. Pte. Ltd.
- Patankar, S. V. (1980), *Numerical heat transfer and fluid flow*, Hemisphere, New York.
- Precht, E., U. Franke, L. Polerecky, and M. Huettel (2004), Oxygen dynamics in permeable sediments with wave-driven pore water exchange, *Limnol. Oceanogr.*, **49**(3), 693–705.
- Soulsby, R. L., and R. J. S. Whitehouse (2005), Prediction of ripple properties in shelf seas, *Tech. rep.*, U.S. Office of Naval Research.
- Stegner, A., and J. E. Wesfreid (1999), Dynamical evolution of sand ripples under water, *Phys. Rev. E*, **60**(4), R3487.
- Styles, R., and S. M. Glenn (2000), Modeling stratified wave and current bottom boundary layers on the continental shelf, *J. Geophys. Res.*, **105**(C10), 24,119–24,139.
- Testik, F. Y., S. I. Voropayev, and H. J. S. Fernando (2005), Adjustment of sand ripples under changing water waves, *Phys. Fluids*, **17**(7), 072104, doi:10.1063/1.1946768.
- Testik, F. Y., S. I. Voropayev, S. Balasubramanian, and H. J. S. Fernando (2006), Self-similarity of asymmetric sand-ripple profiles formed under nonlinear shoaling waves, *Phys. Fluids*, **18**(108), 108101, doi:10.1063/1.2362859.
- Tjerry, S. (1995), Morphological calculation of dunes in alluvial rivers, Ph.D. thesis, Det Naturvidenskabelige Fakultet Kbenhavns Universitet.
- Tjerry, S., and J. Fredsøe (2005), Calculation of dune morphology, *J. Geophys. Res.*, **110**, F04013, doi:10.1029/2004JF000171.
- Traykovski, P. (2007), Observations of wave orbital scale ripples and a nonequilibrium time-dependent model, *J. Geophys. Res.*, **112**, C06026, doi:10.1029/2006JC003811.
- Traykovski, P., A. E. Hay, J. D. Irish, and J. F. Lynch (1999), Geometry, migration, and evolution of wave orbital ripples at LEO-15, *J. Geophys. Res.*, **104**(C1), 1505–1524.
- van Rijn, L. C. (1993), *Principles of Sediment Transport in River, Estuaries and Coastal Seas*, Aqua Publications, Amsterdam.
- Vittori, G., and P. Blondeaux (1990), Sand ripples under sea waves: Part 2. Finite-amplitude development, *J. Fluid Mech.*, **218**, 19–39.
- Voropayev, S. I., G. B. McEachern, D. L. Boyer, and H. J. S. Fernando (1999), Dynamics of sand ripples and burial/scouring of cobbles in oscillatory flow, *Appl. Ocean Res.*, **21**, 249–261.
- Wiberg, P. L., and C. K. Harris (1994), Ripple geometry in wave-dominated environments, *J. Geophys. Res.*, **99**(C1), 775–789.
- Wilcox, D. C. (1988), Reassessment of the scale-determining equation for advanced turbulence models, *ALAA J.*, **26**(11), 1279–1310.
- Zedler, E. A., and R. L. Street (2001), Large eddy simulation of sediment transport: Currents over ripples, *J. Hydraul. Eng. - ASCE*, **127**, 444–452.
- Zijlema, M. (1996), On the construction of a third-order accurate monotone convection scheme with application to turbulent flows in general domains, *Int. J. Numer. Methods Fluids*, **22**, 619–641.

F. Ardhuin, Service Hydrographique et Océanographique de la Marine, Brest, France.

P. Bonneton and V. Marieu, Université Bordeaux 1, CNRS, UMR 5805-EPOC, avenue des facultés, Talence, F-33405 France. (v.marieu@epoc.u-bordeaux1.fr)

D. L. Foster, Department of Civil and Environmental Engineering and Geodetic Science, Ohio State University, 470 Hitchcock Hall, 2070 Neil Avenue, Columbus, OH 43210, USA.